Slotted hydrofoil design optimization to minimize cavitation in amphibious aircraft application: A numerical simulation approach

Fernando Roca Conesa[1a] and Rhea Patricia Liem[*2]

[1]Universitat Politècnica de València, Camino de Vera s/n, Valencia 46022, Spain
[2]Department of Mechanical and Aerospace Engineering,
The Hong Kong University of Science and Technology, Hong Kong

Abstract. The proposed study aims to numerically investigate the performance of hydrofoils in the context of amphibious aircraft application. In particular, we also study the effectiveness of a slotted hydrofoil in minimizing the cavitation phenomenon, to improve the overall water take-off performance of an amphibious aircraft. We use the ICON A5 as a base model for this study. First, we propose an approach to estimate the required hydrofoil surface area and to select the most suitable airfoil shape that can minimize cavitation, thus improving the hydrodynamic efficiency. Once the hydrofoil is selected, we perform 2D numerical studies of the hydrodynamic and cavitating characteristics of a non-slotted hydrofoil on ANSYS Fluent. In this work, we also propose to use a slotted hydrofoil to be a passive method to control the cavitation performance through the boundary layer control. Numerical results of several slotted configurations demonstrate notable improvement on the cavitation performance. We then perform a multiobjective optimization with a response surface model to simultaneously minimize the cavitation and maximize the hydrodynamic efficiency of the hydrofoil. The optimization takes the slot geometry, including the slot angle and lengths, as the design variables. In addition, a global sensitivity study has been carried and it shows that the slot widths are the more dominant factors.

Keywords: slotted hydrofoil; cavitation inhibition; passive flow control; RSM optimization

1. Introduction

Amphibious aircraft can take-off and land on both water and conventional runways on ground. One of the main advantages in developing amphibious aircraft lies in the ability to operate where it is impractical to build airports and runways. As an example, amphibious aircraft can help transport passengers and cargo to places with waterways or coastlines but no airports, and will be useful in regions with many islands. In addition, amphibious aircraft can be used in emergency situations such as rescue missions and aerial firefighting, as well as for recreation purposes. Normally, amphibious aircraft need to take-off in a short distance (e.g., rivers, ports), so attention must be paid to take-off performance.

∗Corresponding author, Ph.D., E-mail: rpliem@ust.hk
[a]M.Sc., E-mail: ferroco1etsid@gmail.com

One of the main amphibious aircraft design challenges is to reduce water take-off distance. In this work, we aim to investigate the effectiveness of using hydrofoils, by mounting them below the aircraft hull, in addressing this challenge. A hydrofoil is essentially a lift generating device similar to an airfoil but works underwater. This device can provide extra lift and reduce hull resistance during the water take-off by getting the hull out of the water sooner, allowing a faster take-off with a shorter distance. By lifting the hull out of the water, the aircraft needs to only overcome the drag on the foils and not the total hull resistance, thus allowing a higher rate-of-climb.

Despite some performance advantages mentioned above, designing an efficient hydrofoil for amphibious aircraft applications comes with several challenges. Moreover, existing studies are limited as previous studies mainly focused on ship designs and marine applications, and none on amphibious aircraft. Petrie (1966) presented some of the problems encountered during the development of the United States Navy's first hydrofoil ship. During the testing of the ship in 1961, it was found that there was cavitation damage in the aft propellers due to separation off the upper surface of the hydrofoil. Cavitation occurs when water pressure drops below the vapour pressure of the working liquid. When this phenomenon appears, the hydrofoil no longer generates enough lift, which can lead to a catastrophic impact of the amphibious aircraft onto the water. As velocity increases during take-off, the pressure on the upper surface of the hydrofoil decreases and may drop below the sea water vapour pressure, leading to cavitation. This phenomenon also affects the structural integrity of the hydrofoil by causing vibrations, erosion, noise problems which could lead to safety problems. In addition, the hydrodynamic drag increases with cavitation, so it can lead to a significant performance deterioration. Therefore, preventing cavitation is the primary consideration in the design of the hydrofoil system and it is the main scope of the present study.

Flow separation control and boundary layer control are two boundary layer management methods aimed to reduce cavitation and improve the performance. Boundary layer control methods can be divided into passive or active methods. The active flow separation control requires additional energy for the boundary layer control. A variable sweep hydrofoil (Mercier (1969)) is an active method which can be used to improve hydrodynamic and cavitation performance. Among the active methods, cavitating flow control through continuous tangential mass injection through a slot channel in the guided vanes section surface of a hydrofoil was proposed by Timoshevskiy *et al.* (2016) to reduce substantially the amplitude and suppress the periodic cavity length oscillations and pressure pulsations. On the other hand, vortex generators are passive flow control solutions. An appendage located on the hydrofoil wall was proposed by Mortezazadeh *et al.* (2014) as a passive method to decrease the size of the bubble during cavitation phenomena and control the boundary layer over the hydrofoil. Hydrofoil steering vanes and surface texture variation were proposed by Hilleman (2005) to reduce underwater drag and cavitation reduction. The use of a slot to control the boundary layer, which is investigated in this research, is another passive flow control solution. The slotted hydrofoil was first introduced by NASA (Somers (2012)) in airfoils to increase the laminar flow region over the airfoil and thus, achieve a drag reduction for business-jet applications. Other researchers, such as Belamadi *et al.* (2016), have applied this passive method to improve the aerodynamic performance of wind turbine blades, but the first application of this passive method into hydrofoils was performed by Wei *et al.* (2015). In their study, they used a vice foil to improve cavitation and hydrodynamic performance by optimizing the position of the vice foil, assuming a fixed slot geometry. However, they did not focus on the design of the slot itself nor on the influence of the design parameters on the hydrofoil's performance.

The list of the boundary layer control methods provided is not exhaustive. One key advantage of a passive method is that it does not need an external mechanism for its operation which could

substantially reduce the manufacturing cost and time. In other words, a passive control does not require auxiliary power or a control loop, which reduces design complexity and component weight. The present work focuses on a numerical investigation of a slotted hydrofoil to minimize cavitation and improve the hydrodynamic performance. In particular, the study is done in the context of amphibious aircraft design and applications. Different slot locations, slot widths and angles are studied to achieve this objective for a hydrofoil for amphibious aircraft applications using numerical 2D simulations.

This paper is organized as follows. Section 2 highlights amphibious aircraft design challenges and complexities. Section 3 describes an iterative method used to estimate the hydrofoil surface and the criteria followed to select the airfoil shape for the hydrofoil. Section 4 introduces in detail the numerical analysis for the amphibious aircraft hydrofoil. The corresponding results are shown and discussed in Section 5. Section 6 proposes a slotted hydrofoil to improve cavitation performance and shows the numerical results. A numerical multi-objective optimization research is done in Section 7. Concluding remarks are then given in Section 8.

2. Amphibious aircraft design challenges and highlights of contributions

The unique capabilities of amphibious aircraft to operate both in water and on land, while providing versatility and competitive advantages to conventional ground-based aircraft, impose significant challenges in its design and development. Despite the rapid development during the First and Second World Wars (Qiu and Song (2016)), it stagnated in the 1950s (Canamar (2012)) and still lags behind the development of ground-based aircraft (Qiu and Song (2013)).

The early development of amphibious aircraft relied mainly on experimental water tank tests and empirical methods (Qiu and Song (2013)), and thus lacked mathematical rigor. As such, a thorough design exploration and optimization was not possible (Thurston (1995), Thurston and Vagianos (1970)). Moreover, the studies mainly focused only on one design aspect and thus failed to address the trade-offs between different design considerations. As an example, the shorter beam required to reduce drag might reduce lateral stability and was studied by Shoemaker and Parkinson (1933). A small depth of the step in an amphibious aircraft hull that could reduce drag resistance during water take-off would be suboptimal at high speeds (Bell (1935)). While numerical optimization has been commonly used in aircraft design since the late 1970s (Hicks *et al.* (1974), Jameson (1990, 1998)), its application in amphibious aircraft is still limited. Qiu and Song (2016) recently performed a response-surface-based multiobjective optimization to find the optimum hull step configuration, achieving an 18% improvement in take-off distance without sacrificing cruise performance substantially. Puorger *et al.* (2007) performed an aerostructural optimization for a fire-extinguisher amphibious aircraft, focusing mainly on the ground effect during low-altitude cruise, without any water take-off considerations. These optimizations, however, did not consider the use of hydrofoils in their design considerations.

The addition of hydrofoils to the hull design has been explored to provide faster climb and cruise (Gudmundsson (2013)), though many studies were terminated early as they could not perform a thorough design exploration and optimization (Thurston and Vagianos (1970)). A hydrofoil is essentially a lifting surface that works underwater, like an airfoil in air. Experiments showing the effectiveness of hydrofoils in improving the take-off efficiency of seaplanes dated as early as 1861 by Thomas Moy (King (1966)), and in 1907 and 1914 by the Wright brothers (Thurston and Vagianos (1970)). To the best of our knowledge, however, there have not been any

rigorous numerical studies to assess the effectiveness of hydrofoils in improving amphibious aircraft operation. The co-author has previously conducted a preliminary investigation (Seth and Liem (2018)) relevant to the use of hydrofoils in amphibious aircraft design, focusing on the analyses of water take-off. The water take-off performance analysis results showed that the hydrofoil helped reduce hull resistance during water take-off, shortening the time taken to lift the hull out of the water. However, the hydrofoil increased the aerodynamic drag once it was out of the water due to cavitation, further motivating the work presented in this paper.

Amphibious aircraft design needs to strike the right balance between its aerodynamic and hydrodynamic performances, which further complicates the aircraft design process. In this work, we focus on numerically investigating the hydrofoil design to simultaneously improve the hydrodynamic performance, quantified in terms of the lift-to-drag (L/D) ratio, and minimize the cavitation effect, specifically in the context of amphibious aircraft design. The highlights of the design challenges addressed in this work, and the proposed solutions, are summarized below.

1. Hydrofoil selection and sizing to satisfy the required water take-off performance

Due to the complexity and interdisciplinary nature of an aircraft system, an aircraft design process is a highly complex process that needs to be performed iteratively. Designing a hydrofoil that can satisfy the required water take-off performance also requires an iterative process that simultaneously considers its aerodynamic performance (wing lift) and hydrodynamics performance (both hydrofoil and hull lift). Our proposed iterative process is elaborated in Section 3 of this paper.

2. Time averaging the unsteady flow characteristics

The pressure fluctuations caused by cavitation (Seol (2013)) led to fluctuations in the lift and drag as well (Hong *et al.* (2017)). To evaluate and compare the lift-to-drag ratios of various cavitation numbers, we perform the time averaging based on the cloud cavitation shedding frequency, which will be described in detail in Section 5.

3. Slotted hydrofoil numerical study as a passive boundary layer control method

Our study, presented in Section 6, shows that slotted hydrofoils can further reduce the cavitation effect which can potentially improve the water take-off performance of an amphibious aircraft. The water take-off analysis, however, is beyond the scope of this paper.

3. Iterative hydrofoil selection and sizing design approach

A hydrofoil refers to a wing structure mounted on a strut below the amphibious aircraft. This lift-generating device is used to lift the hull out of the water during water take-off and allows a hull resistance reduction and a notable increase in the rate-of-climb. To size and design the hydrofoil, the ICON A5 amphibious aircraft is used as a baseline design in this study. ICON A5 is a high-wing monoplane with its wing and fuselage made up of carbon-fibre material. Its Dornier-style sponsons provide a high hydrodynamic stability. To determine the most suitable foil shape for the hydrofoil, an iterative method has been proposed. ICON A5 specifications can be found in Table 1. In this study, we only consider untapered hydrofoils for simplicity.

The hydrofoil surface area is obtained through an iteration process, by ensuring the consistency between the aerodynamic performance obtained from the solver XFOIL and the kinematic equation. In particular, we focus on the vertical force components as the vertical acceleration of the amphibious aircraft plays an important role during take-off. This kinematic equation is derived based on the Newton's second law, as shown in Eq. (1), which states that during take-off, the lift

Table 1 ICON A5 main specifications[a]

Weight (kg)	686
Airfoil surface (m^2)	13.46
Stall speed -clean flaps- (m/s)	20.06
Take-off distance (m)	256
Take-off speed (m/s)	24

provided by the hydrofoil (L_h) and wing (L_w) minus the weight (W) of the amphibious aircraft is equal to the amphibious aircraft mass (m) multiplied by the vertical acceleration (a).

$$L_h + L_w - W = ma \tag{1}$$

The water take-off procedure can be decomposed into several stages. Before the amphibious aircraft starts to rotate, i.e., when the aft hull is free from water, the amphibious aircraft reaches the hump speed. The hump speed is defined at the point when the hull waterline tends to stagnate, and when the static buoyant force and hydrodynamic drag force reach the maximum value. Shortly after the amphibious aircraft reaches the hump speed, a rapid disappearance of the hull buoyant force occurs (Wei *et al.* (2015)). Since cavitation phenomenon tends to appear at a high speed (after the hump speed), the buoyancy is neglected in Eq. (1), since the buoyancy force would be relatively small compared to the other lift contributions at this stage. The lift of the hydrofoil and wing is provided by Eqs. (2) and (3), respectively.

$$L_h = \frac{1}{2}(V_{TO})^2 C_{Lh} S_h \rho_{water} \tag{2}$$

$$L_w = \frac{1}{2}(V_{TO})^2 C_{LTO} S_w \rho_{air} \tag{3}$$

The lift coefficient of the wing at take-off condition, C_{LTO}, can be obtained by Eq. (4), using the ICON A5 specification on stall speed provided in Table 1.

$$V_{TO} = 1.2 \ V_{Stall} = \sqrt{\frac{2W_{TO}}{C_{LTO} S_w \rho_{air}}} \tag{4}$$

Because the take-off distance, speed, and the final altitude of the amphibious aircraft are known, it is possible to obtain the vertical acceleration during take-off by assuming a uniformly accelerated rectilinear motion. Therefore, we are left with the lift coefficient of the hydrofoil C_{Lh} (which strongly depends on the angle of attack, α) as the unknown in Eq. (1). Since we assume that there is no taper ratio, the hydrofoil area only depends on the chord and span. We can obtain this through an iterative process. We first calculate the Reynolds number with Eq. (5), and then calculate the corresponding C_{Lh} using XFOIL at a fixed α=3°.

$$Re = \frac{\rho_{water} V_{TO} c}{\mu_{water}} \tag{5}$$

---

[a]Data available online at http:// www.planeandpilotmag.com/article/icon-a5/ [retrieved 10 May 2018].

Table 2 Hydrofoil chord, span and C_L at take-off condition for each foil after the iteration process

Parameters and Foils	ClarkY	NACA 0009	NACA 63412	YS930	S1223	AH217	E818	E851	HQ259b	HQ309	HQ2195	MH121	MH122
Hydrofoil chord (cm)	14.19	15.46	12.18	12.65	7.99	12.98	10.57	11.6	10.49	12.12	12.17	11.55	10.61
Hydrofoil span (cm)	24.7	50	30	30	20.1	30	32	33	34.5	28	32.5	29	28
C_L (take-off)	0.717	0.325	0.688	0.662	1.566	0.646	0.744	0.657	0.694	0.741	0.636	0.751	0.846

Table 3 Hydrofoil performance parameters for each foil after the iteration process (absolute values)

Parameters and Foils	ClarkY	NACA 0009	NACA 63412	YS930	S1223	AH217	E818	E851	HQ 259b	HQ309	HQ 2195	MH121	MH122
$|C_{Pmin}(3°)|$	1.077	1.225	1.092	1.590	1.963	1.246	2.715	1.820	1.131	1.044	1.143	1.753	1.232
$C_L/C_D(3°)$	123.43	59.49	126.53	96.41	129.57	101.59	76.83	80.12	110.10	128.85	104.23	86.12	130.12
$|C_L/C_{Pmin}(3°)|$	0.666	0.266	0.630	0.416	0.798	0.519	0.272	0.361	0.614	0.710	0.556	0.429	0.683
$|\Delta_{CPmin}$ vs $\alpha(\%)|$	17.36	32.61	34.58	44.77	6.66	27.92	40.79	47.37	30.24	24.48	30.14	43.83	35.42

The XFOIL code combines a panel method and an integral boundary layer formulation for the analysis of potential flow around the airfoils. We perform several iterations (with different chord values) until we obtain the convergence between the Reynolds number computed using Eq. (5) and the one used in XFOIL to obtain the C_{Lh}. Reynolds number is considered as a convergence parameter of the iteration process, since it is an input in XFOIL to obtain the C_{Lh} (viscous analysis) and it is also a parameter that relates the unknowns in Eq. (1) with the results obtained from XFOIL viscous code.

Several types of foils have been studied to determine the most suitable design to minimize cavitation and improve the hydrodynamic efficiency. In particular, we include the following foils in the study: Clark-Y, NACA 0009, NACA 63-412, YS-930, Selig S1223, AH21-7, E-818, E-851, HQ,309, HQ-2195, MH-121 and MH-122. These foil types had previously been used in hydrodynamic applications (Shen *et al.* 1981, Oller *et al.* 2016, Garg *et al.* 2017 and Rozhdestvensky 2006). Table 2 lists the chord and span lengths of the above hydrofoil types, which are obtained after the aforementioned iterative process converges. With this information, we can perform a viscous flow simulation in XFOIL to obtain C_{Pmin}, C_L/C_D, C_L/C_{Pmin} and X_{CPmin} for each airfoil at a range of angles of attack ($-3° \leq \alpha \leq 10°$). To prevent cavitation, which is our main design requirement, the local pressure of the whole upper surface of the hydrofoil must be higher than the vapor pressure. In other words, the minimum pressure coefficient (C_{Pmin}) of the hydrofoil must be higher than a certain value.

To determine the most suitable foil for our reference amphibious aircraft, four parameters have been evaluated: C_{Pmin}, C_L/C_D, C_L/C_{Pmin} and Δ_{CPmin} vs α. All these parameters have been evaluated at an angle of attack of $\alpha = 3°$, which is assumed to be the angle of attack during take-off. The first parameter listed is relevant to assess which hydrofoil is closer to cavitation phenomena at take-off condition. The C_L/C_D ratio is a measure of the hydrodynamic efficiency and thus, this parameter has a high influence on the take-off performance. C_L/C_{Pmin} provides a measure of the decrease of the pressure, and, correspondingly, the tendency to cavitation, when the lift increases. Finally, Δ_{CPmin} vs α provides the rate of decrease of minimum pressure coefficient with the increase of angle of attack. The importance of Δ_{CPmin} vs α is set higher among all the study parameters, because the angle of attack could increase easily during take-off due to wave impacts,

or other external phenomena. This could in turn decrease the minimum pressure coefficient, leading to cavitation and consequently a loss of lift, vibrations, and erosion. Therefore, it is important to consider how much the pressure would decrease as the angle of attack increases. Table 3 shows the absolute value of these four parameters for each foil studied. The value of $|C_{Pmin}|$ should be as low as possible to prevent cavitation. A high C_L/C_D ratio is preferred, as it represents a high hydrodynamic efficiency. The value of $|C_L/C_{Pmin}|$ is more beneficial when it is as high as possible. Finally, the value of $|\Delta_{CPmin}$ vs $\alpha|$ is better to be kept minimum, to prevent minimum pressure drop as the angle of attack increases.

Δ_{CPmin} vs α has been calculated as the variation rate of C_{Pmin} between angles of attack 3° and 4°. Since S1223 airfoil approximately starts to stall at around α≈5°, the interval 3°- 4° has been chosen to evaluate Δ_{CPmin} vs α parameter. As can be seen from Table 3, the values of C_L/C_D are considered to be very high. This may be due to the fact that XFOIL uses a combination of linear vorticity strength distribution with constant source strength on each panel in order to provide transpiration velocity values for viscous solver, therefore the accuracy of the results is limited by the panel resolution as stated by Illiev (2017). Moreover, the transpiration velocities obtained from the potential flow code are essential to model sheet cavitation as stated by Phoemsapthawee *et al.* (2012) and sheet cavitation may appear during take-off conditions. Despite these limitations, the trade-off between accuracy and computational cost of XFOIL is deemed suitable for preliminary and conceptual design phases.

As can be observed from Table 3, foil S1223 has the lower value of $|\Delta_{CPmin}$ vs $\alpha|$, and a higher value of $|C_L/C_{Pmin}|$, making it a good candidate for the foil selection. However, this airfoil goes into stall conditions at a relatively low angle of attack of 5°, which could compromise the take-off performance, and thus this foil is rejected. Other potential candidates include HQ-309 or Clark-Y as they have good hydrodynamic performance and a good behavior in preventing cavitation. Even though HQ-309 airfoil has a lower value of $|C_{Pmin}$ (3°)$|$, it is more sensitive to changes in C_{Pmin} when the angle of attack increases. At an angle of attack of 5°, for instance, $|C_{Pmin}|$ is higher in HQ-309 airfoil than in Clark-Y, which means that it is closer to cavitation. We thus select Clark-Y as the best option among all the foils studied and will be used for the remaining of this paper.

4. Hydrofoil CFD simulation analysis

The unsteady behaviour of cavitating flows and cavity shedding attract much attention during hydrofoil design stages since it can seriously affect the hydrodynamic performance and hydrofoil integrity. Cavitation flow around a hydrofoil is often a multiphase flow associated with turbulence, unsteady flows, and phase change. Many researches have been carried out to simulate the cavitation flow and significant progress has been made in recent years. There have been concerted efforts both in experimental and numerical simulation fronts to perform cavitation research. While performing experiments are important to describe characteristic features of the cavitating flow and to validate numerical simulations, its high cost and dependence on scale models often render such experiments impractical. Some previous work, however, has been performed to validate numerical simulation procedures to be used in subsequent analyses (Homa and Wróblewski 2016, Zhao and Wang 2018, Homa *et al.* 2018, Liu *et al.* 2019). CFD simulations have been shown to be an effective means to analyse the cavitating behaviour successfully by coupling suitable cavitation and turbulence models (Wei *et al.* 2015). In order to investigate the cavitation performance of the Clark-Y hydrofoil, we perform numerical 2D simulations in ANSYS Fluent.
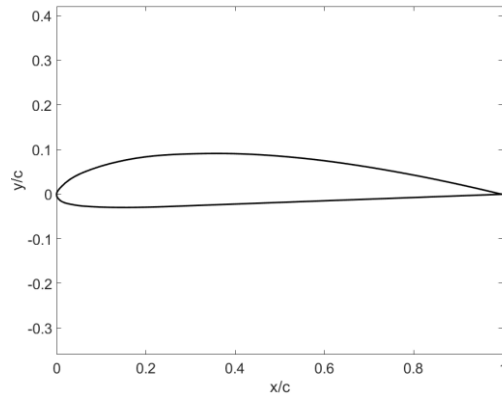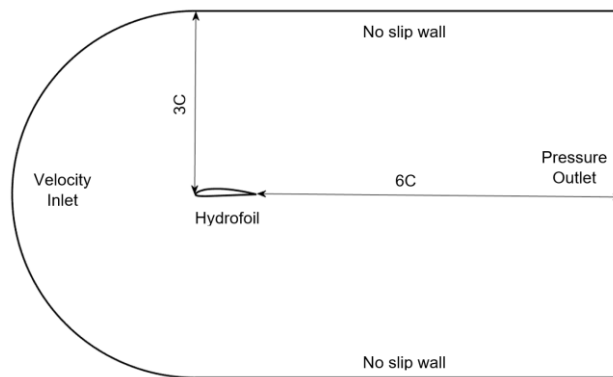
Fig. 1 Clark-Y hydrofoil geometry

Fig. 2 Outline of the 2D computational domain indicating the boundary condition types

4.1 Numerical setup

Fig. 1 shows the hydrofoil shape which will be evaluated in ANSYS Fluent. The computational domain and boundary conditions are illustrated in Fig. 2. The analysis is performed at an angle of attack of 3°, which corresponds to its take-off condition. The computational domain stretches 3 chord lengths upstream (radius) and 6 chord lengths downstream. The inlet boundary condition is the specified take-off speed (24 m/s). The upper and lower boundaries are modelled as non-slip walls. The outlet is a constant pressure boundary condition defined by the cavitation number. The foil itself is assumed to have a non-slip wall. Previous works with Clark-Y hydrofoil, both experimental and numerical, have proven that the computational domain and boundary conditions used are appropriate to simulate cavitation phenomena under these flow conditions (Huang *et al.* 2012, 2013 and Wang *et al.* 2001).

Because of the unsteady characteristics of a cavitating flow, the selection of the turbulence model is critical for an accurate cavitation modelling. The numerical model solves the unsteady Navier-Stokes equations, coupled with the SST k-ω turbulence model, following the work by Qiu and Song (2013), with automatic near-wall treatment which can automatically switch from wall

functions to a low-Reynolds near wall formulation as the mesh is refined[b]. Many studies (both experimental and computational) with Clark-Y hydrofoil (Homa and Wróblewski 2016, Zhao and Wang 2018, Homa *et al.* 2018, Liu *et al.* 2019) have shown that the SST k-ω turbulence model is suitable and adequate to simulate under this flow conditions, which validates the selection of this turbulence model in the work presented in this paper.

Unsteady simulations are carried out to capture the cavitation dynamics. A first order implicit transient formulation is used for the time-dependent computation. In the unsteady simulations, the time step is set as $\triangle t = 4.1 \times 10^{-6}$ s, which is chosen to assure an average Courant-Friendrichs-Lewy (CFL) number of $U_\infty \triangle t / \triangle x = 1$, where $\triangle x$ refers to the smallest grid size. In order to keep the balance between efficiency and computational accuracy, we limit the number of iterations to 20 at each time step (Hong *et al.* 2017).

The solving strategy used is the unsteady SIMPLE algorithm. PRESTO! and QUICK schemes in ANSYS are used for pressure and vapour phase transport equation, respectively. To obtain an accurate resolution of the cavitation, second order discretization schemes are used for density, momentum, turbulent kinetic energy, and dissipation rate. A least-squares-cell-based method is used to compute the gradients of the variables appearing in the governing equations. The calculations were performed on a workstation equipped with 12 cores computing nodes Intel®Xeon® E5-2603, 1.6 GHz CPU, and 128 GB of RAM.

4.2 Cavitation characterization

A cavitation phenomenon is typically characterized by a non-dimensional parameter called the cavitation number (σ), as shown in Eq. (6). This parameter is used to evaluate the potential of a flow for cavitation. In Eq. (6), p_V is the vapor pressure (which was set to 3540 Pa), ρ is the working liquid density, p_{ref} is the reference hydrostatic pressure and V is the freestream flow velocity.

$$\sigma = \frac{p_{ref} - p_V}{\frac{1}{2}\rho V^2} \tag{6}$$

Every flow, whether cavitating or not, can be attributed to a cavitation number. The cavitation number depends on geometry, fluid temperature and inflow velocity (Šarc *et al.* (2017)). Four different cavitation regimes can be observed in the flow over a body, namely the incipient, sheet, cloud, and supercavitation. Experiments performed by Wang *et al.* (2001) provided comprehensive information about cavitation dynamics and cavitating flow structures under these four cavitation regimes. In cloud cavitation regime the vapour phase covers a subsection of the body (Roohi *et al.* (2013)). The conditions at which cavitation first appears (the incipient regime) are described in Eq. (7) as stated by Garg *et al.* (2017), where the pressure coefficient C_p is provided by Eq. (8), and p_{local} refers to the local fluid pressure. Lowering the value of the cavitation number will lead to the appearance of cavitation or when cavitation already exists, it will be extended.

$$\sigma + C_p \leq 0 \tag{7}$$

---

[b]ANSYS Fluent documentation available online at https://www.sharcnet.ca/Software/Ansys/17.0 [retrieved 10 May 2018].

$$C_p = \frac{p_{local} - p_{ref}}{\frac{1}{2}\rho V^2} \tag{8}$$

Essentially, cavitation modelling methods can be classified into two main groups: one-fluid and two-fluid models. In two-fluid models, the conservation equations of discrete and continuous phases are solved separately, which makes them computationally expensive. In one-fluid models, the conservation equations (mass and momentum) for the mixture are solved by considering the flow as a mixture of two phases (Homa 2014).

Works by Homa and Wróblewski (2016) and Liu *et al.* (2019) have shown that the Schnerr-Sauer model is more suitable than the Kunz or Merkle models to simulate cavitation flow over Clark-Y hydrofoil under this flow conditions. The Schnerr-Sauer model can accurately capture small bubbles and vortices generated during cavitation process as well as simulate cavitation growth and shedding that agrees with experimental data in cloud cavitation regime.

Based on these findings, the Schnerr-Sauer model is used to simulate the cavitation in this work, assuming a thermal equilibrium between the liquid and vapor phases. This model expresses the vapour fraction as a function of the radius of the bubbles, which is assumed to be the same for all bubbles. The governing equations that describe the cavitation process involve a two-Eulerian phases system, where it is assumed that there is thermal equilibrium between all components and phases, and no-slip conditions between any phases. In this work, two parameters are used to describe cavitation. The first one (Eq. (7)) indicates when incipient cavitation regime appears. In addition, the vapour volume fraction is used as an indicator of the appearance of the cloud cavitation regime.

4.3 Grid generation and independence study

In numerical simulations, the quality of the computational mesh has a great influence on the accuracy of the numerical results. The mesh should have adequate fineness to ensure the validity of the results. Moreover, the mesh size near the wall plays an important role on the cavitation dynamic analysis. The computational domain is divided into two different zones, as shown in Fig. 3 and 4. The first zone contains the hydrofoil's surface with a structured mesh. A large number of mesh elements are located near the hydrofoil surface to accurately capture the gradients in the boundary layer as well as the cavitation dynamics. In the second zone, an unstructured mesh is used. In addition, a finer mesh is also implemented downstream, to increase the analysis accuracy and thus better capture the evolution and detachment of the sea water vapour bubbles. The wall functions models need to adjust the thickness of neighboring cells to hydrofoil surface; the height of the first cell is $\triangle y = 1 \times 10^{-4}$ m to ensure that $y^+ \approx 1$, where $y^+ = y u_\tau / v$ is the non-dimensional wall distance (where y is the distance to the wall, u_τ is the friction velocity in the wall and v is the local kinematic viscosity of the fluid). To take full advantage of SST k-ω turbulence model it is necessary to guarantee that $y^+ \approx 1$, according to the ANSYS Fluent Theory Guide (2017). In the far-field area, the mesh resolution becomes progressively coarser since the flow gradients approach zero. In addition, to model the evolution of the cavitation bubbles, a finer mesh is located close to the hydrofoil's leading and trailing edges. Fig. 5 shows mesh details for the slotted hydrofoil. As can be seen, significantly finer mesh is used in areas close to the surface for a more accurate analysis result.
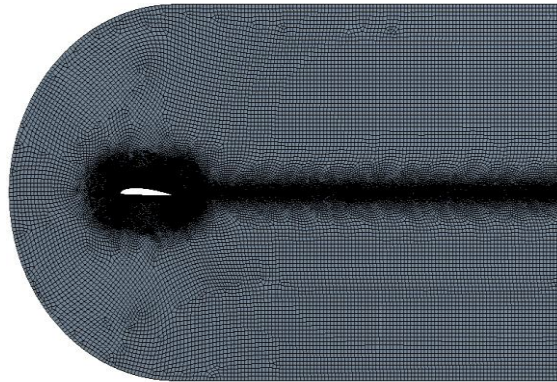
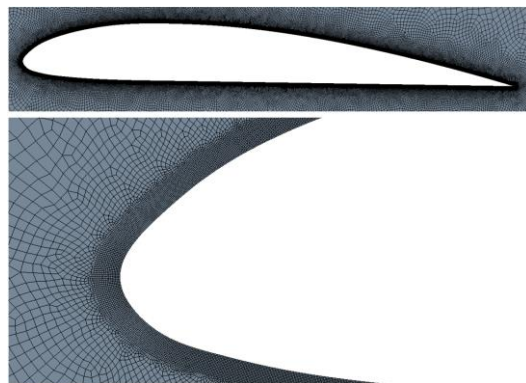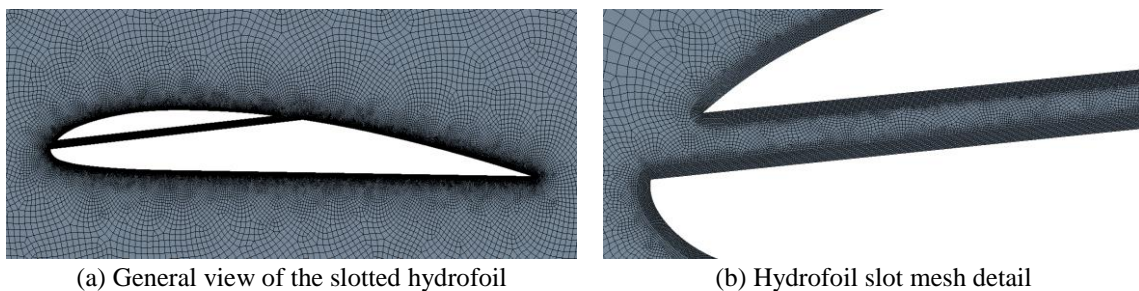Fig. 3 General view of Clark-Y hydrofoil grid

Fig. 4 Hydrofoil and leading-edge mesh detail

(a) General view of the slotted hydrofoil   (b) Hydrofoil slot mesh detail

Fig. 5 Slotted hydrofoil mesh detail, with finer mesh closer to the surface

We look into the convergence of lift and drag coefficients values for the mesh independence study. The mesh convergence is analysed based on the computations in the case of $\sigma = 0.7$ and $\alpha = 3°$ on five sets of meshes with different resolution, as listed in Table 4. At the cloud cavitation regime, i.e., where $\sigma = 0.7$, we observe some specific features including vapour cloud shedding at the end of the cavity. The wall distance of the first layer of grid nodes closest to the hydrofoil wall was set as 1×10^{-4} m for all the meshes. A grid independence analysis has been done only for the non-slotted hydrofoil configuration for two main reasons: (i) for all configurations studied, the same domain size has been maintained; the modifications done only on hydrofoil surface (slot),

Table 4 Results of the mesh independence analysis by evaluating the values of time-averaged lift and drag coefficients ($\overline{C_L}$, $\overline{C_D}$)

Grid	Elements	Nodes	$\overline{C_L}$	|Error (%)|	$\overline{C_D}$	|Error (%)|
Very coarse	29965	30576	0.54681	-	0.03677	-
Coarse	51158	51914	0.52879	3.41	0.03301	11.37
Medium	88733	90210	0.51888	1.91	0.03345	1.29
Fine	109974	111919	0.53354	2.75	0.03369	0.74
Very fine	150812	153503	0.53070	0.53	0.03366	0.09

and (ii) for the configuration with slot, a higher number of cells was used to mesh the slot walls and to assure that $y^+ \approx 1$, as can be observed from Fig. 5.

To perform the mesh independence study, we evaluate the convergence of the time-averaged lift and drag coefficients ($\overline{C_L}$, $\overline{C_D}$), since the cloud cavitation regime is not steady. The absolute percentage changes are also calculated for these values. As can be inferred from Table 4, the difference between the predicted time-averaged lift and drag coefficient results decreases with increasing number of grid nodes. Table 4 shows that between the fine and very fine mesh the percentage change can be considered negligible for both coefficients. Therefore, for the purpose of saving computational resources and time, the fine mesh is used in all subsequent calculations. The fine mesh provides a good compromise between accuracy and computational burden. As mentioned before, the fine mesh is also referenced as the base of the grid generation of the slotted hydrofoil.

5. Cavitation performance study and discussion

The time-averaged lift and drag coefficients of the Clark-Y hydrofoil for the range of cavitation numbers between 0.7 (cloud cavitation regime) and 2.5 (non-cavitation) are illustrated in Fig. 6. The time-averaged coefficients are calculated by considering all instantaneous results within one cavitation period, to take into account the unsteady characteristics of cavitation.
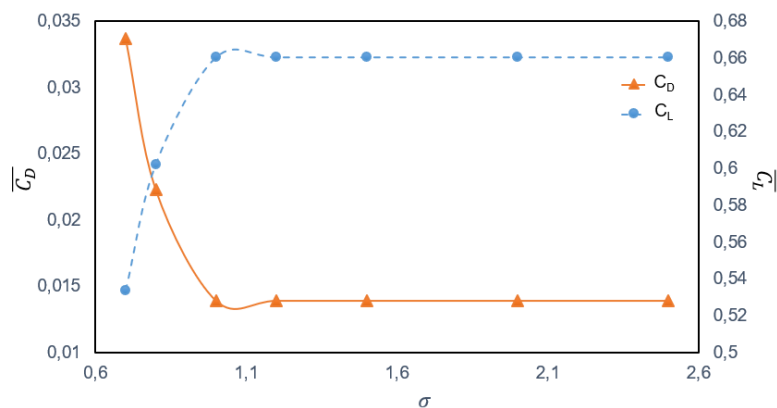

Fig. 6 Time averaged lift and drag coefficients as function of cavitation number, covering the cloud cavitation and non-cavitation regimes
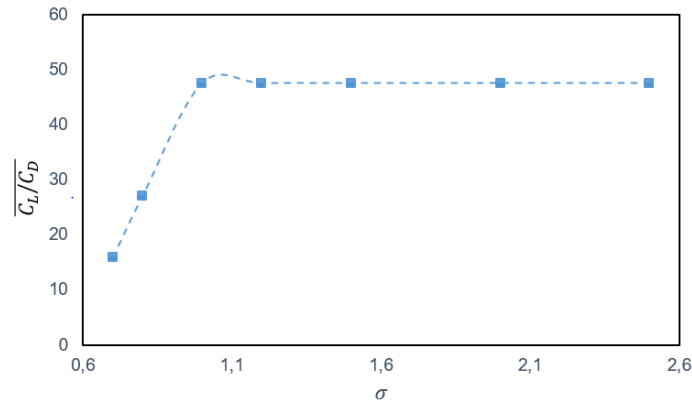
Fig. 7 Averaged lift-to-drag ratio as a function of cavitation number, which shows a drop in hydro-dynamic efficiency due to the onset of cloud cavitation (at σ < 0.8)

To determine the shedding frequency of the cavitation phenomenon, we propose to apply a Fast Fourier Transform (FFT) to the lift and drag coefficients. Fig. 7 shows the averaged L/D ratio $(\overline{C_L}/\ \overline{C_D})$ for the same range of cavitation numbers to observe the variation of the hydrodynamic efficiency with the cavitation number. When the flow is non-cavitating, i.e., when the cavitation numbers are larger than 1.2, both the lift and drag time-averaged coefficients remain relatively unchanged as the cavitation number is varied, and thus the L/D ratio also remains constant, as shown in Fig. 7.

In the cavitation inception stage, where cavitation numbers range between 0.9 and 1.2, the net effect of cavitation on the time-averaged lift and drag coefficients is insignificant. We observe that there is a slight increase in the lift coefficient caused by the travelling bubbles in the inception cavitation stage. Further decreasing the cavitation number leads to the appearance of the sheet cavitation regime, which results in an increase of the drag coefficient and a decrease in the lift coefficient. This implies a notable decrease in the L/D ratio, and thus a deterioration of the hydrodynamic performance. When the cavitation number drops below 0.8, the cloud cavitation regime appears. In this regime, the vortex shedding, and related flow unsteadiness strongly affects the flow structure around the hydrofoil, where the drag coefficient reaches its maximum value and the lift coefficient reaches its minimum, leading to a sharp deterioration of the hydrodynamic efficiency. In this study, we exclude the supercavitation regime in the analysis since it is only relevant at a high speed, which is outside the operating regime of the take-off procedure of an amphibious aircraft, studied in this paper.

5.1 Time-dependent visualization of cloud cavity

We focus our study on the flow condition with the most adverse hydrodynamic efficiency, which is when the cavitation number is around 0.7. In this section, we further analyze this cloud cavitation regime of the Clark-Y hydrofoil. Cloud cavitation is an undesirable phenomenon which significantly degrades the hydrodynamic performance and results in noise, erosion, and undesirable vibrations.

Fig. 8 illustrates the time evolution of the lift and drag coefficients. Both the lift and drag coefficients are shown to exhibit periodic behavior. Fig. 9 shows the time evolution of the sea
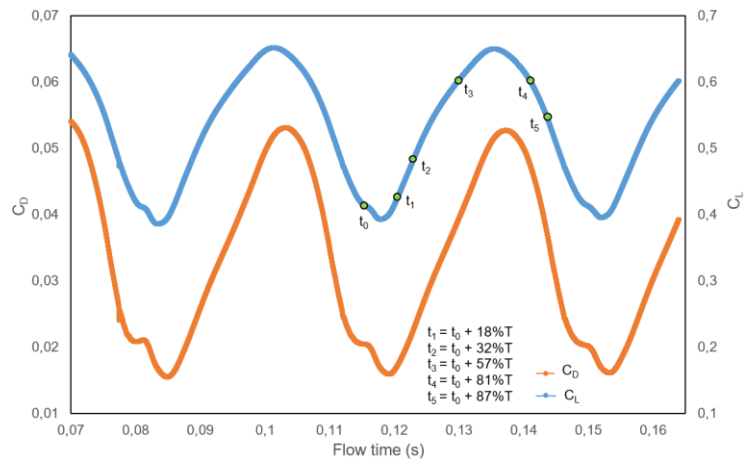
Fig. 8 Lift and drag coefficients evolution over flow time at the cloud cavitation regime
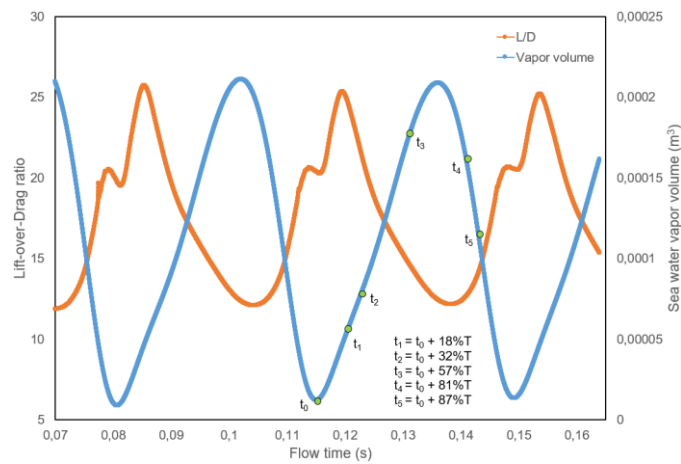

Fig. 9 Sea water vapor volume and L/D evolution over flow time at the cloud cavitation regime
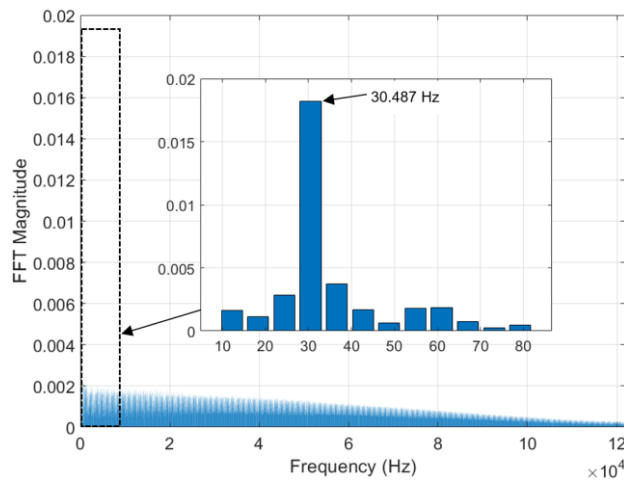

Fig. 10 Fast Fourier Transform (FFT) of the C_L coefficient and detail of shedding frequency

water vapor volume and L/D ratio values with flow time. As can be observed, the sea water vapor volume variation is periodic and correlates well with the evolution of L/D. When the instantaneous values of the sea water vapor volume are maximum, the hydrodynamic efficiency reaches its minimum value. Therefore, we can infer that the presence of cloud cavitation sharply deteriorates the hydrodynamic performance of the hydrofoil.

To determine the major vortex-shedding frequency of the cavity phenomenon, a Fast Fourier Transform (FFT) can be applied to the time-history of the lift and drag coefficients, using a prime-factor algorithm. Essentially, the Fourier transform enables taking the time-dependent data and resolving it into an equivalent summation of sine and cosine waves. Fig. 10 shows the FFT analysis for the C_L time-history, where the C_L FFT magnitude is plotted in the ordinate axis. The magnitude (or amplitude) is the square root of the power spectral density (i.e., is the distribution of signal power in the frequency domain). By analyzing Fig. 10, we can obtain the cavity shedding frequency, which is 30.487 Hz and a Strouhal number of $St = fc/V_\infty = 0.1804$ (where f is the shedding frequency and c denotes the hydrofoil chord).
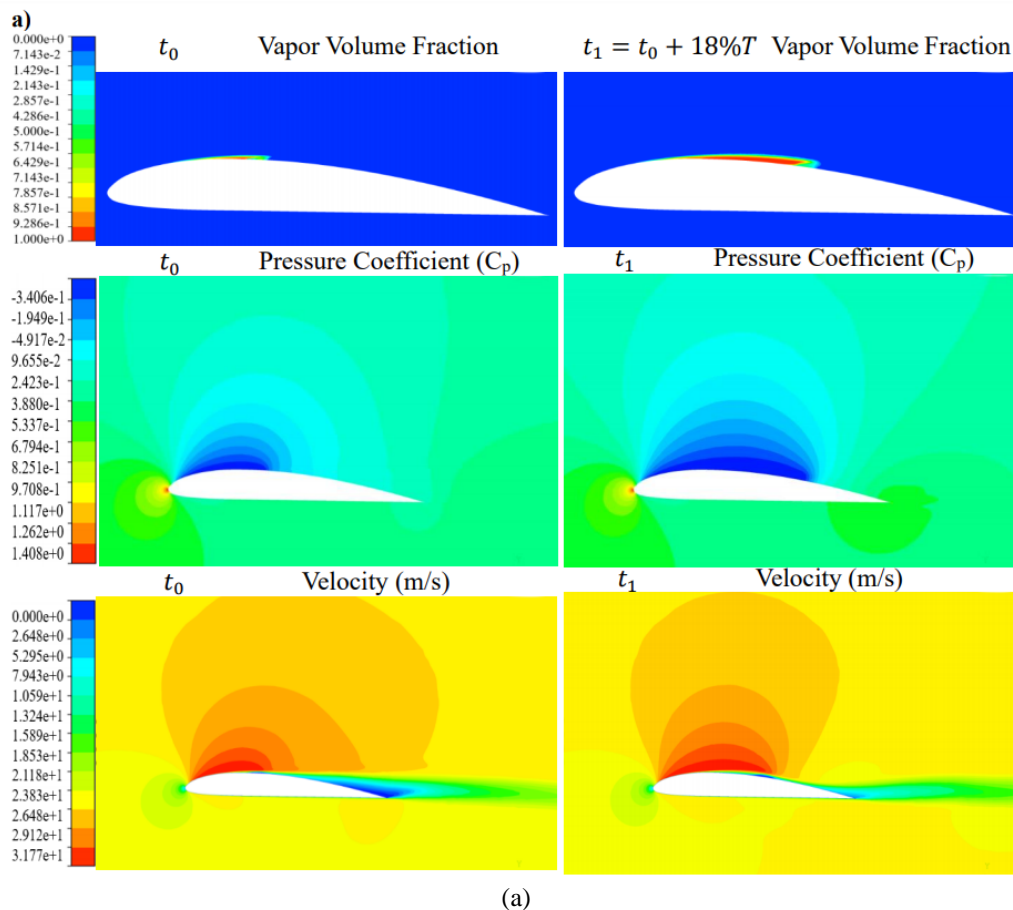

(a)

Fig. 11 (a) Vapour volume fraction, velocity magnitude, and pressure coefficients contours evolution over one cavitation cycle from (t_0 - t_1) for cavitation number σ=0.7 (cloud cavitation regime)
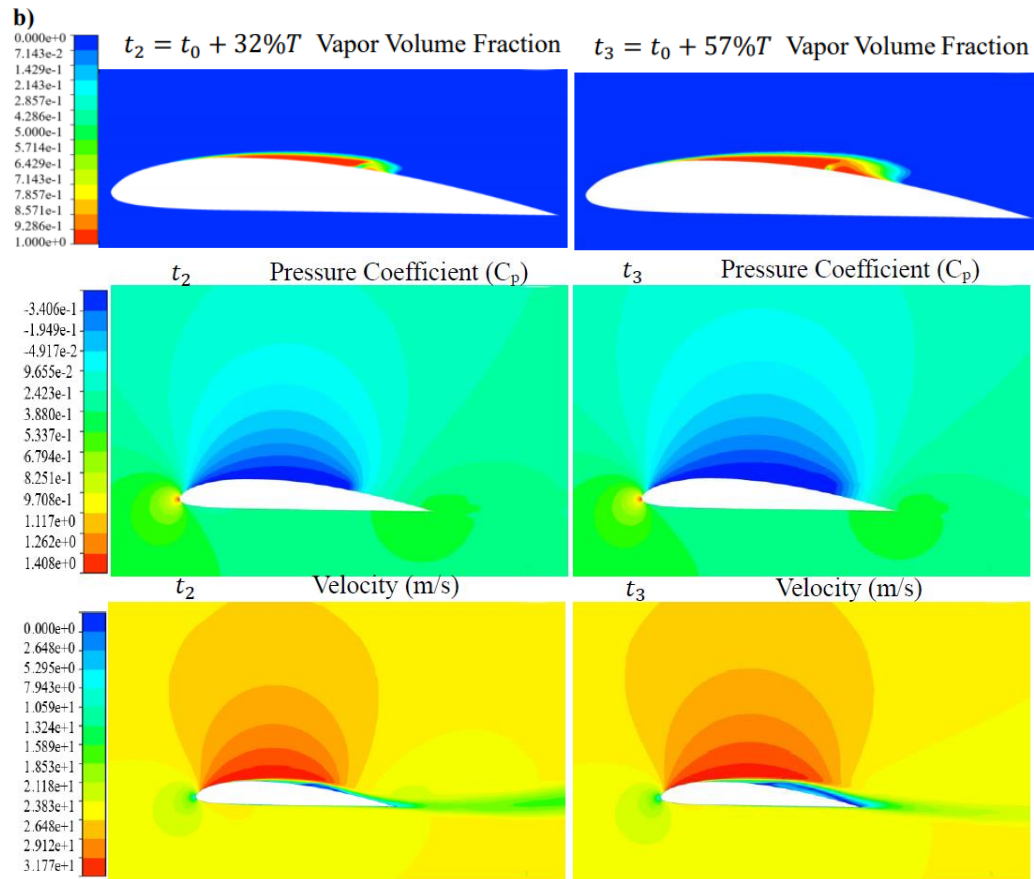
Fig. 11 (b) Vapour volume fraction, velocity magnitude, and pressure coefficients contours evolution over one cavitation cycle from (t_2 - t_3) for cavitation number σ=0.7 (cloud cavitation regime)

The cavity period is extracted from the shedding frequency as $T = 1/f = 0.0328$ s. From the cavity period it is possible to obtain the time-averaged lift and drag coefficients. To further evaluate the temporal evolution of the cavity structures and its consequences on the hydrodynamic performance, the vapor volume fraction, velocity magnitude and pressure coefficient are studied over one cavitation cycle, i.e., from t_0 to t_5. The time sample points are expressed in percentage terms of the cavity period (as shown in Figs. 8 and 9). Fig. 11 (a)-11(c) show the results of these analyses. Special attention needs to be paid to the correlation between the evolution of the vapour volume fraction velocity magnitude and the pressure coefficient distribution along the hydrofoil surface, which will be discussed shortly.

As can be inferred from Fig. 11(a), at t_0 the presence of the vapor volume fraction over the hydrofoil surface is restricted to about one-third of the chord length. At t_0, there is also a region of low velocity at the rear part of the hydrofoil, which is directly related to the relatively high-pressure area at the end of the foil. As can be seen from Fig. 8, at t_0 the vapor volume around the hydrofoil is minimum. From periods t_0 to t_1, we can observe that the presence of the vapor volume fraction has increased to half of the chord length. The growth in the vapor volume fraction region goes hand in hand with the decrease of the C_P values over the hydrofoil surface. In addition, it can
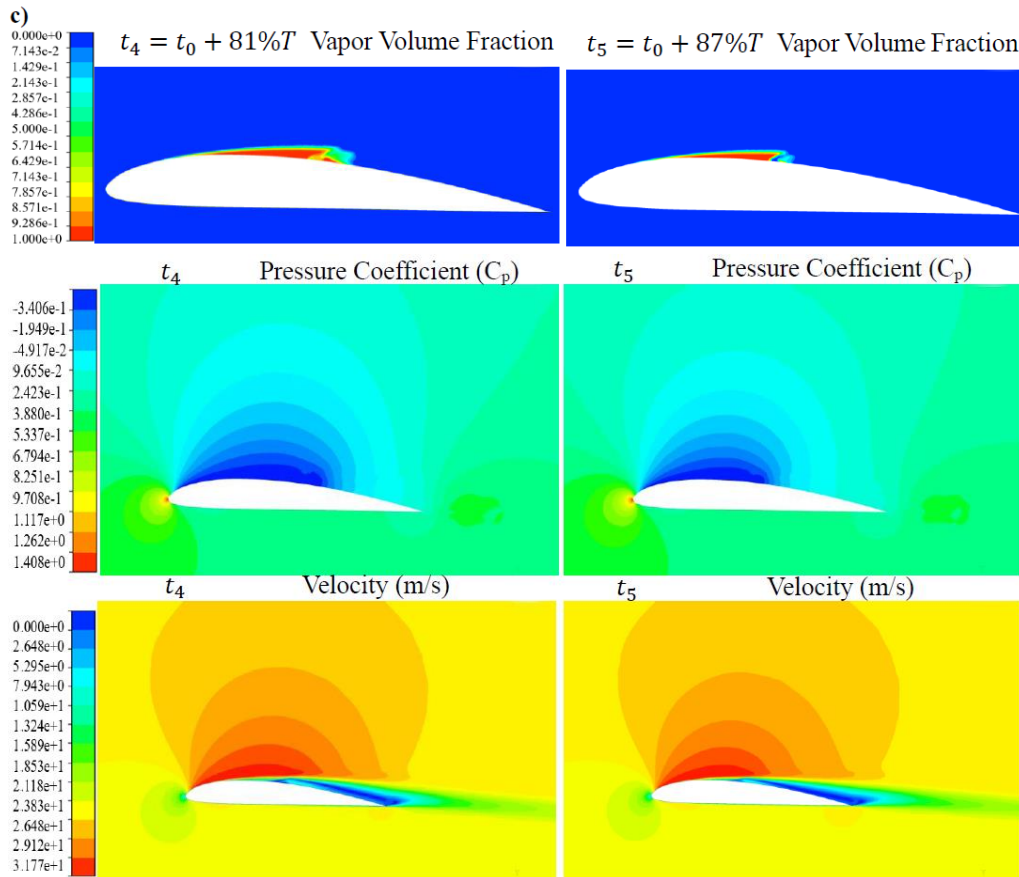
Fig. 11 (c) Vapour volume fraction, velocity magnitude, and pressure coefficients contours evolution over one cavitation cycle from (t_4 - t_5) for cavitation number $\sigma=0.7$ (cloud cavitation regime)

be observed that from periods t_0 to t_1, the region of zero velocity magnitude (blue color) is displaced towards the trailing edge of the hydrofoil and a zone of high velocity (red color) appears at half of the hydrofoil chord length.

When the cavity growth is more than half of the chord length (periods from t_2 to t_3), a re-entrant jet directed towards the hydrofoil leading edge appears (i.e. the pressure coefficient decreases along the rear part of the hydrofoil upper surface, accompanied by a region of zero velocity magnitude). The cavity structures are strongly affected by this re-entrant jet and it leads to the formation of a bubbly two-phases mixture that breaks off from the rear part. In particular, we can observe a bubbly detachment during the period between t_2 and t_3. The bubbly detachment can be seen when there are two regions of flow with vapor volume fraction equal to one (red color) separated by a region of less vapor volume fraction value. The re-entrant jet causes the cavitation cloud to separate (at this point the maximum size of the attached part of the cavity is reached). The separated cloud travels downstream and collapses in the higher-pressure region. As can be seen from Fig. 11 (b), between periods $t_2 - t_3$ there is a considerably growth in the cavity length over the hydrofoil, and thus, in the vapor volume fraction; this increment is associated with a drastic decay in the L/D ratio (i.e. hydrodynamic efficiency). So, it can be inferred that during the appearance of

the re-entrant jet the take-off performance will be adversely affected. It is also necessary to mention that during the bubbly detachment, undesirable vibrations appear, and could affect both the structural integrity and passengers' comfort. In addition, this bubbly detachment could lead to hydrofoil erosion.

Although there is still a cavity attached to the hydrofoil upper surface (close to the leading edge in periods t_4 and t_5), it diminishes drastically due to the push effect caused by the relatively high pressure downstream. Between periods t_4 and t_5, we observe that the cavity has reduced its presence to half of the chord. From Fig. 9 it can be seen that between periods t_4 and t_5, the vapor volume diminishes considerably. A similar behavior is observed in the pressure coefficient. After t_5, the almost-vanished cavity regrows after the collapse, exhibiting the same cyclic behavior. These results suggest that the re-entrant jet is the main physical mechanism that affects and controls the dynamics (growth and collapse) of the cloud cavitation regime.

6. Slotted hydrofoil numerical study

We have previously shown that the cloud cavitation regime affects the hydrodynamic performance of the hydrofoil which can lead to a poor take-off performance, as well as undesirable vibrations. In order to modify the flow structure which appears during cavitation phenomenon, control the bubble size, and prevent erosion, we propose to use a slotted hydrofoil as a passive boundary layer control. Fig. 12 describes the three design parameters of the slot.

The angle θ allows to control the point where the flow coming from the freestream region arrives at the hydrofoil upper surface and thus modifies the cavitation flow structures. In addition, parameters L1 and L2 allow modification of the width of the slot and thus, to control the flow rate injected to the hydrofoil upper surface. Numerical simulations are carried using the same setup described for the non-slotted configuration and the same domain dimensions and boundary conditions. As described in Section 3.3, the same mesh is used. However, a finer mesh has been
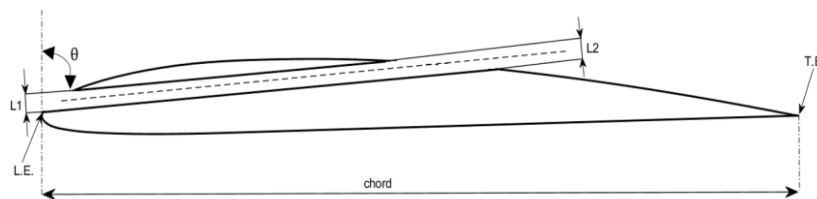

Fig. 12 Slot geometric characteristics (L.E.: leading edge, T.E.: trailing edge, θ: slot angle, L1 and L2: lower and upper slot widths)

Table 5 Summary of the slotted/non-slotted hydrofoil numerical study

Configuration	L1 (m)	L2 (m)	θ (°)	$\overline{L/D}$	$\Delta_{\overline{L/D}}$(%)	Max. V_f	Δ_v(%)
Reference case	-	-	-	15.83	-	2.09e-04	-
Parallel slot	0.0007	0.0007	88.64	17.22	8	6.84e-05	-67.27
Convergent I	0.0025	0.0016	88.96	18.02	12	8.53e-05	-59.19
Convergent II	0.0025	0.0014	76.31	18.72	15	6.63e-05	-68.28
Divergent	0.0006	0.0016	76.52	15.41	-3	4.13e-05	-80.24

used through the slot wall to assure that $y^+ \approx 1$ and thus, take full advantage of the of SST k-ω formulation. Moreover, FFT is applied to the C_L and C_D time-history in order to obtain the shedding frequency, to enable calculating the time-averaged lift and drag coefficients.

We analyse the influence of slot locations, slot widths and angles on the cavitation performance by varying their values in the numerical simulations. Table 5 summarizes the main configurations tested. We use the averaged L/D ratio to assess the hydrodynamic performance of the hydrofoil. As can be seen, all slotted configurations except the divergent configuration analysed improve the averaged L/D ratio in comparison to the reference case (non-slotted hydrofoil) through the reduction of the vapour volume fraction (V_f) and modification of the boundary layer.

From Table 5 we can see that the hydrodynamic and cavitation performance of the slotted hydrofoil is highly affected by the position of the slot. The results presented in Table 5 suggest that the divergent configuration is the least suitable in terms of improving the hydrodynamic performance. This is due to the fact that for incompressible flow in a divergent duct, the pressure increases but the velocity decreases, which significantly reduces the vapour volume fraction but at the expense of a poor averaged L/D ratio. In other words, the fluid passing through the slot does not have sufficient kinetic energy to re-energize the inner region of the boundary layer, where the main cavity structures appear.

From Table 5, it can be inferred that the convergent slot configurations can achieve a higher averaged L/D ratio. Moreover, the effect of the slot in the vapour volume fraction reduction is affected by the slot angle θ, due to the fact that the injection of fluid to re-energize the boundary layer is more effective near the point where the re-entrant jet appears, i.e., where the bubbly two-phase mixture breaks off. In the flow conditions analyzed, the re-entrant jet appears when the cavity length is more than half of the chord length (the periods from t_2 to t_3 shown in Fig. 11 (b)). So, in the convergent II configuration, θ is lower than in convergent I configuration, which means that the injection of the fluid occurs earlier than that in convergent I configuration. That is the reason why the convergent II configuration performs better than the convergent I configuration (i.e., achieves a better hydrodynamic performance as well as a higher vapor volume fraction reduction). As can be seen from Table 5, the three design parameters used have an important role in the cavitation performance, and a variation in only one of them may cause a change in the cavitation behavior of the slotted hydrofoil. In order to identify the optimum configuration and the role of these three design parameters, numerical studies involving an optimization and sensitivity numerical study will be carried in the next section.

7. Slotted hydrofoil optimization numerical study

We have previously shown that the three design parameters (θ, L1 and L2) have important effects on both cavitation and hydrodynamic performance of slotted hydrofoils. In order to investigate the optimum configuration of these parameters, we perform an optimization procedure to maximize the hydrodynamic efficiency and improve the cavitation performance of the slotted hydrofoil. A Response Surface Model (RSM) is used to represent the objective function. RSM is a set of mathematical and statistical techniques that are used for empirical model building. RSM is well suited to applications with small numbers of design variables and computational expensive objective functions evaluations (Khuri and Mukhopadhyay (2010)). The accuracy of the RSM approximate model depends mainly on the selection of sample points. An Optimal Space Filling algorithm (OSF) is used for the design of experiments (DOE). An OSF design is essentially a Latin
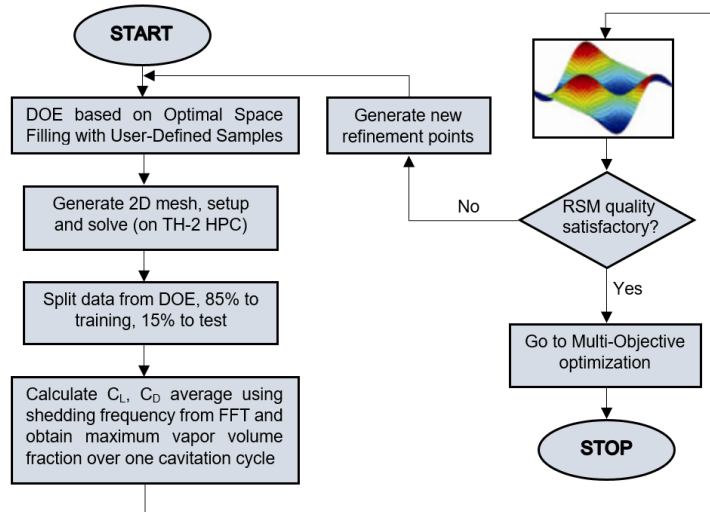
Fig. 13 Flowchart slotted hydrofoil design optimization with a response surface model

Table 6 Coefficient of determination and root mean square error of the RSM

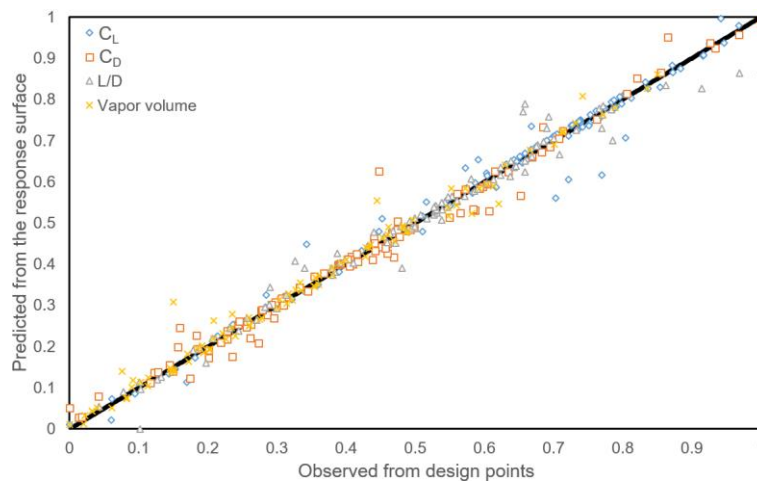| Study parameter	$\overline{C_L}$	$\overline{C_D}$	$\overline{C_L}/\overline{C_D}$	Vapor volume
Coefficient of determination (R^2)	0.97644	0.97608	0.96832	0.9868
Root mean square error	0.0046439	0.00067281	0.53441	4.2111e-6

Fig. 14 Predicted versus observed normalized values, which shows that the response surface model has a good predictive accuracy

Hypercube design that is optimized through several iterations, maximizing the minimum distance between any two design points to achieve a more uniform distribution across the design space (Jin *et al.* (2005)). 85% of the points from the DOE are used as building points for the RSM and the remaining 15% are used to validate the model. In total, 100 points were used to build the RSM. CFD simulations were carried out at all simulation points using the same approach, setup

and boundary conditions as described in Section 3. The numerical simulations were performed parallelly on the Tianhe-2 supercomputer located in the National Supercomputer Center in Guangzhou using its ANSYS 19.0 Linux version. The RSM is applied according to the approach illustrated in the flowchart of Fig. 13.

The value ranges of the design parameters are:

$$75° \leq \theta \leq 90°$$

$$0.0003 \ m \leq L_1 \leq 0.003 \ m$$

$$0.0003 \ m \leq L_2 \leq 0.003 \ m$$

An RSM is constructed using a non-parametric regression (NPR) algorithm. The NPR algorithm is a metamodeling technique prescribed for predictably high nonlinear behaviour of the outputs. From the numerical simulations, we observe that a small variation in the design parameters can drastically change the hydrodynamic and cavitation behaviour (see Table 5). Due to this noisy and nonlinear response, we decide to use an NPR algorithm rather than kriging or low order polynomials (Yakowitz and Szidarovszky (1985)). Table 6 shows the coefficient of determination (R^2) and the root mean square error of the response surface model.

Fig. 14 shows the normalized predicted values from the RSM versus those obtained from running CFD simulations. This plot indicates the accuracy of the RSM, i.e., the closer the points are to the diagonal line, the better the response surface fits the points. As can be seen, the RSM maintains a good fitting accuracy for all simulation's points.

After the RSM is constructed, a systematic multi-objective optimization is carried out using a Multi-Objective Genetic Algorithm (MOGA). The MOGA used is a hybrid variant of the popular non-dominated sorted genetic algorithm-II (NSGA-II) based on the controlled elitism concepts. MOGA leads to an accurate identification of the Pareto front (Chiandussi *et al.* (2012)). However, a large computational effort is needed to identify the Pareto front. The Pareto ranking scheme is done by a fast, non-dominated sorting method. Penalty functions or Lagrange multipliers are not needed due to the fact that the constraint handling uses the same non-dominance principle as the objectives.

The objective functions and constraints for the optimization problem formulation are given as follows:

$$\text{Minimize} \begin{cases} -\left(\overline{\dfrac{C_L}{C_D}}\right)_{(L1,L2,\theta)} \\ V_{f(L1,L2,\theta)} \end{cases}$$

$$\text{Subject to: } \overline{\frac{C_L}{C_D}} \geq \left(\overline{\frac{C_L}{C_D}}\right)_{\text{Reference case}}, \ V_f \leq \left(V_f\right)_{\text{Reference case}}$$

To evaluate the effectiveness of the design, we use the hydrodynamic efficiency and the sea water vapor volume of the non-slotted hydrofoil as the reference. In the optimization, we put more emphasis to maximize averaged L/D than to minimize the vapor volume, and the values have to be better than those of the non-slotted hydrofoil (i.e., the reference case). In MOGA, the maximum allowable Pareto percentage is set to 80% as the convergence criterion. This value represents the ratio of the number of desired Pareto points to the number of samples per iteration. The number of initial populations, and the number of populations at each iteration are set to 10000.

After the optimization is performed, a sensitivity study is carried out to gain insight into how the variations of design variables affect the variations of the output variables ($\overline{C_L}$, $\overline{C_D}$, $\overline{L}/\ \overline{D}$ and
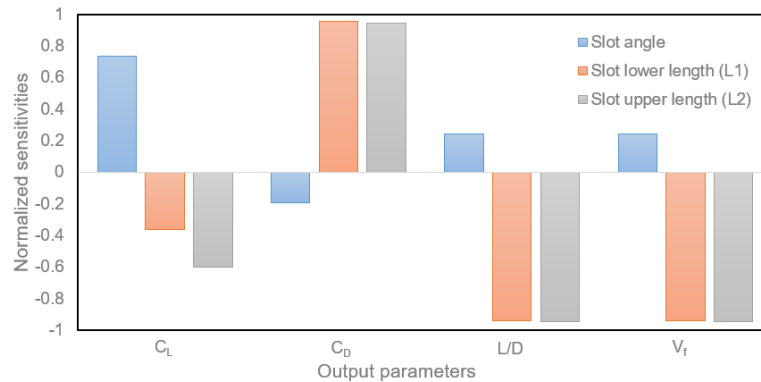
Fig. 15 Global sensitivity study

Fig. 16 Geometry of the optimized slotted hydrofoil

Table 7 Final design parameters of the optimized slotted hydrofoil

Slot angle (θ)	Lower length (L1)	Upper length (L2)
83.8°	0.0022152 m	0.0016945 m

Table 8 Performance comparison between the reference case (non-slotted hydrofoil) and the optimized slotted hydrofoil

	$\overline{L/D}$	$\Delta(\%)$	Maximum V_f	$\Delta(\%)$
Reference case	15.835	-	0.00020872	-
Optimized slot	22.64	42.97	0.00004906	-76.5

V_f). Fig. 15 shows the results of the global sensitivity study. As can be inferred from Fig. 15, the slot angle (θ) significantly affect the lift coefficient, but its impacts on the rest of the output parameters are relatively low. The upper and lower slot widths, on the other hand, have high influences on $\overline{C_D}$, $\overline{L}/\overline{D}$ and V_f. As such, in order to improve the hydrodynamic and cavitation performance of the hydrofoil, attention must be paid to the slot widths rather than in the slot angle. The upper and lower slot widths control the flow injection to the inner region of the boundary layer, where the main cavity structures occur.

Fig. 16 shows the geometry of the optimized slotted hydrofoil after the multi-objective optimization. The final optimized design parameters are shown in Table 7. The final optimum design performance is compared with the reference case (see Table 8). Not only is the optimized slotted hydrofoil able to inhibit the cavitation appearance, it also can improve the averaged hydrodynamic performance. In the optimum configuration, the hydrodynamic performance is improved by 42.97% and the maximum vapor volume is reduced by 76.5%.

8. Conclusions

In this paper, we have discussed some of the design challenges of a hydrofoil for amphibious aircraft applications, focusing on the cavitation performance and its adverse consequences during take-off performance. Numerical studies were performed to simulate the cavitation performance of Clark-Y hydrofoil under a range of cavitation numbers. The Fast Fourier Transform (FFT) of the time-dependent lift and drag coefficient values were used to obtain the cavity shedding frequency and to compute the time-averaged lift and drag coefficients over one cavitation period for different cavitation numbers.

A further study of the cloud cavitation regime was performed, which showed that the evolution of the cavitation structures was correlated with the pressure distribution along the hydrofoil surface. In addition, we also observed that the main mechanism of the cavity bubbles breakage in the cloud cavitation regime was caused by the re-entrant jet. Modifications of the boundary layer could change the cavity evolution. Based on this argument, we proposed a passive boundary layer control method to inhibit cavitation. Three design parameters were used to determine the slot location and dimension. Numerical results showed that the slotted configuration not only could inhibit cavitation, its boundary layer control mechanism could also improve the hydrodynamic performance. By performing a numerical optimization procedure using a response surface model technique, we verified that the slotted hydrofoil achieved better hydrodynamic and cavitation performances than the non-slotted hydrofoil, which was treated as the reference case. A global sensitivity study of the design parameters was also performed and the results showed that the dominant parameters to inhibit cavitation and improve the performance are the upper and lower slot width geometries. The results presented in this paper supported the hypothesis that the slotted hydrofoil could improve take-off performance by minimizing cavitation. Hydrofoil structural analyses are currently beyond the scope of the present paper. Further studies need to be performed to study the impact of the slots to the structural performance of the hydrofoils, prior to implementing hydrofoils in amphibious aircraft applications.

Acknowledgments

References

ANSYS Fluent (2017), ANSYS Fluent Theory Guide, ANSYS Inc., Southpointe, Canonsburg, Pennsylvania, U.S.A.

Belamadi, R., Abdelouaheb, D., Adrian, I. and Ramzi, M. (2016), "Aerodynamic performance analysis of slotted airfoils for application to wind turbine blades", *J. Wind Eng. Industr. Aerodyn*., **151**, 79-99. https://doi.org/10.1016/j.jweia.2016.01.011.

Bell, J.W. (1935), "The effect of depth of step on the water performance of a flying-boat hull model", Technical Report No. 535, National Advisory Committee for Aeronautics (NACA), Washington, U.S.A.

Canamar, A. (2012), "Seaplane conceptual design and sizing", M.Sc. Thesis, University of Glasgow, Soctland, U.K.

Chiandussi, G., Codegone, M., Ferrero, S. and Varesio, F.E. (2012), "Comparison of multi-objective optimization methodologies for engineering applications", *Comput. Math. Appl.*, **63**(5), 912-942. https://doi.org/10.1016/j.camwa.2011.11.057.

Garg, N., Gaetan, K.K.W., Joaquim, R.R.A.M. and Yin L.Y. (2017), "High-fidelity multipoint hydrostructural optimization of a 3-D hydrofoil", *J. Fluids Struct.*, **71**, 15-39. https://doi.org/10.1016/j.jfluidstructs.2017.02.001.

Gudmundsson, S. (2013), *General Aviation Aircraft Design: Applied Methods and Procedures, Appendix C3: Design of Seaplanes*, (1st Edition), Butterworth-Heinemann, U.S.A.

Hicks, R.M., Murman, E.M. and Vanderplaats, G.N. (1974), "An assessment of airfoil design by numerical optimization", Technical Report NASA TM X-3092, California, U.S.A.

Hilleman, T.B. (2005), "Apparatus and method for reducing hydrofoil cavitation", Patent number: US 2005/0076819 A1.

Homa, D. (2014), "Comparison of different mathematical models of cavitation", *Trans. VŠB Tech. Univ. Ostrava Mech. Ser.*, **60**(2).

Homa, D. and Wróblewski, W. (2016), "Numerical research on unsteady cavitating flow over a hydrofoil", *J. Phys. Conf. Ser.*, **760**, 012006.

Homa, D., Wróblewski, W., Majkut, M. and Strozik, M. (2018), "Experimental and numerical investigation of cavitation on Clark-Y foil", *J. Phys. Conf. Ser.*, **1101**, 012008.

Hong, F., Yuan, J. and Zhou, B. (2017), "Appplication of a new cavitation model for computations of unsteady turbulent cavitating flows around a hydrofoil", *J. Mech. Sci. Technol.*, **31**(1), 249-260. https://doi.org/10.1007/s12206-016-1227-x.

Huang, B., Wang, G., Yu, Z. and Shi, S. (2012), "Detached-eddy simulation for time-dependent turbulent cavitating flows", *Chin. J. Mech. Eng.*, **25**(3), 484-490. https://doi.org/10.3901/CJME.2012.03.484.

Huang, B., Young, Y.L., Wang, G. and Shyy, W. (2013), "Combined experimental and computational investigation of unsteady structure of sheet/cloud cavitation", *J. Fluids Eng.*, **135**(7), 071301. https://doi.org/10.1115/1.4023650.

Iliev, S.P. (2017), "Aerofoil analysis using XFOIL - practical implementation for preliminary wing design", Imperial College London, U.K.

Jameson, A. (1998), "Aerodynamic design via control theory", *J. Sci. Comput.*, **3**(3), 233-260. https://doi.org/10.1007/BF01061285.

Jameson, A. (1990), "Automatic design of transonic airfoils to reduce the shock induced pressure drag", *Proceedings of the 31st Israel Annual Conference on Aviation and Aeronautics*, Haifa, Israel.

Jin, R., Wei, C. and Agus S. (2005), "An efficient algorithm for constructing optimal design of computer experiments", *J. Stat. Plan. Infer.*, **134**, 268-287. https://doi.org/10.1115/DETC2003/DAC-48760.

Khuri, A.I. and Mukhopadhyay, S. (2010), "Response surface methodology", *Wiley Interdisciplin. Rev. Comput. Stat.*, **2**, 128-149. https://doi.org/10.1002/wics.73.

King, H.F. (1966), *Aeromarine Origins: The Beginnings of Marine Aircraft, Winged Hulls, Air-Cushion and Air-Lubricated Craft, Planing Boats and Hydrofoils*, (1st Edition), Aero-Publishers.

Liu, Y., Wang, J. and Wan, D. (2019), "Numerical simulations of cavitation flows around Clark-Y hydrofoil", *J. Appl. Math. Phys.*, **7**, 1660-1676. https://doi.org/10.4236/jamp.2019.78113

Mercier, J.A. (1969), *Tests of a Variable Sweep Hydrofoil with Cavitation and Ventilation*, Defense Technical Information Center, U.S.A.

Mortezazadeh, M., Ali, K. and Khodayar J. (2014), "Cavitation control on hydrofoils", *Proceedings of the International Conference on Heat Transfer and Fluid Flow*, Prague, Czech Republic, August.

Oller, S.A., Nallim, L.G. and Oller, S. (2016), "Usability of the Selig S1223 profile airfoil as a high lift hydrofoil for hydrokinetic application", *J. Appl. Fluid Mech.*, **9**(2), 537-542.

Petrie, D.M. (1966), "Operational and developmental experience on the U.S. navy hydrofoil high point", *J. Aircraft*, **3**(1), 79-84. https://doi.org/10.2514/3.59269.

Phoemsapthawee, S., Jean-Baptiste, L., Steven, K. and Jean-Marc, L. (2012), "Implementation of a

transpiration velocity-based cavitation model within a RANSE solver", *Eur. J. Mech. B/Fluids*, **32**, 45-51. https://doi.org/10.1016/j.euromechflu.2011.11.001.

Puorger, P.C., Dessi, D. and Mastroddi, F. (2007), "Preliminary design of an amphibious aircraft by the multidisciplinary design optimization approach", *Proceedings of the 48th AIAA/ASME/ASCE/AHS/ASC Structures, Structural Dynamics, and Materials Conference*, Honolulu, Hawaii, U.S.A.

Qiu, L. and Song, W. (2016), "Efficient multiobjective optimization of amphibious aircraft fuselage steps with decoupled hydrodynamic and aerodynamic analysis models", *J. Aerosp. Eng.*, **29**(3), 04015071. https://doi.org/10.1061/(ASCE)AS.1943-5525.0000557.

Qiu, L. and Song, W.B. (2013), "Efficient decoupled hydrodynamic and aerodynamic analysis of amphibious aircraft water takeoff process", *J. Aircraft*, **50**(5), 1369-1379. https://doi.org/10.2514/1.C031846.

Roohi, E., Amir, P.Z. and Mahmood P.F. (2013), "Numerical simulation of cavitation around a two-dimensional hydrofoil using VOF method and LES turbulence model", *Appl. Math. Model.*, **37**, 6469-6488. https://doi.org/10.1016/j.apm.2012.09.002.

Rozhdestvensky, K.V. (2006), "Wing-in-ground effect vehicles", *Progress Aerosp. Sci.*, **42**(3), 211-283. https://doi.org/10.1016/j.paerosci.2006.10.001.

Šarc, A., Stepišnik-Perdih T., Martin, P. and Matevžˇ, D. (2017), "The issue of cavitation number value in studies of water treatment by hydrodynamic cavitation", *Ultrasonics Sonochem.*, **34**, 51-59. https://doi.org/10.1016/j.ultsonch.2016.05.020.

Seol, H. (2013), "Time domain method for the prediction of pressure fluctuation induced by propeller sheet cavitation: numerical simulations and experimental validation", *Ocean Eng.*, **72**, 287-296. https://doi.org/10.1016/j.oceaneng.2013.06.030.

Seth, A. and Liem, R.P. (2018), "Takeoff analysis on amphibious aircraft with implementation of a hydrofoil", *Proceedings of the World Congress on Advance in Civil, Environmental, and Materials Research*, Incheon, South Korea, August.

Shen, Y.T. and Eppler, R. (1981), "Wing sections for hydrofoils, part 2 non-symmetrical profiles", *J. Ship Res.*, **25**, 191-200.

Shoemaker, J.M. and Parkinson, J.B. (1933), "A complete tank test of a model of a flying-boat hull – N.A.C.A Model no. 11", Technical Report 464. National Advisory Committee for Aeronautics, Washington, U.S.A.

Somers, D.M. (2012), "Design of a slotted, natural-laminar-flow airfoil for business-jet applications", Research Report NASA/CR–2012-217559, Langley Research Center, Pennsylvania, U.S.A.

Thurston, D.B. (1995), *Design for Flying*, 2nd Edition, TAB Books.

Thurston, D.B. and Vagianos, N.J. (1970), "Hydrofoil Seaplane Design" Unclassified Final Report no. 6912 for Naval Air Systems Command under contract N00019-69-0475, Sandford, Maine, U.K.

Timoshevskiy, M.V., Ivan, I.Z., Konstantin, S.P. and Dmitriy, M.M. (2016), "Cavitating flow control through continuous tangential mass injection on a 2D hydrofoil at a small attack angle", *Proceedings of the International Symposium and School of Young Scientists "Interfacial Phenomena and Heat Transfer"*, Russia, November.

Wang, G., Inanc, S., Wei, S., Toshiaki, I. and Shuliang, C. (2001), "Dynamics of attached turbulent cavitating flows", *Progress Aerosp. Sci.*, **37**(6), 551-581. https://doi.org/10.1016/S0376-0421(01)00014-8.

Wei, Q., Chen, H.X. and Rui, Z. (2015) "Numerical research on the performances of slot hydrofoil", *J. Hydrodynam.*, **27**(1), 105-111. https://doi.org/10.1016/S1001-6058(15)60462-0.

Yakowitz, S.J. and Szidarovsky F. (1985), "A comparison of kriging with nonparametric regression methods", *J. Multivariate Anal.*, **16**(1), 21-53.

Zhao, M. and Wan, D. (2018), "Numerical investigation of cloud cavitation flows around Clark-Y hydrofoil", *Proceedings of the 3rd International Symposium of Cavitation and Multiphase Flow*, Shanghai, China, April.

GY